Journal of Power Sources 191 (2009) 111–118

Contents lists available at ScienceDirect

Journal of Power Sources

journal homepage: www.elsevier.com/locate/jpowsour

Study on the microstructure and electrochemical properties of lead–calcium–tin–aluminum alloys

H. Li[a], W.X. Guo[a,b], H.Y. Chen[a,*], D.E. Finlow[c], H.W. Zhou[d], C.L. Dou[d], G.M. Xiao[d], S.G. Peng[d], W.W. Wei[d], H. Wang[d]

[a] School of Chemistry and Environment, South China Normal University, Guangzhou 510006, China[1]
[b] Jewelry Institute of Guangzhou Panyu Polytechnic, Guangzhou 511483, China
[c] Shawnee State University, Portsmouth, OH 45662, USA
[d] Zhuzhou Smelter Group Co., Ltd., Zhuzhou, Hunan 412004, China

ARTICLE INFO

Article history:
Received 22 August 2008
Received in revised form 7 October 2008
Accepted 10 October 2008
Available online 1 November 2008

Keywords:
Lead–calcium alloys
Tin
Calcium
Aluminum
Microstructure

ABSTRACT

A detailed investigation of the effects on the microstructure and electrochemical properties of lead–calcium–tin–aluminum alloys of adding tin and calcium was undertaken. Cyclic voltammetry (CV), linear sweep voltammetry (LSV), and electrochemical impedance spectroscopy (EIS) were used to study the anode electrochemical behavior (such as the growth of lead dioxide, a passive film and the evolution of oxygen) of the lead grid alloy in sulfuric acid solution. The structure and corrosion morphology of the lead alloy were observed and analyzed using a polarizing microscope, scanning electron microscopy (SEM), and energy dispersive spectroscopy (EDS). The experimental results show that the grains gradually became smaller as the content of calcium increased, and the content of tin decreased, in the alloy. The size and shape of grains were related to the ratio of tin to calcium content in the alloys. The linear sweep voltammetry and AC impedance measurements suggested that the preferred ratio of tin to calcium content, *r*, is between 9 and 15, and the optimum range of tin content in the alloys is 0.8–1.1%.

1. Introduction

Lead–calcium (Pb–Ca) alloys were studied as early as 1859, and the first application of these alloys in lead-acid batteries was reported in 1935. Lead–calcium alloys can improve the maintenance-free capability of lead-acid batteries with high hydrogen evolution overpotential [1]. The casting properties of Pb–Ca alloys are poor, however, and the high impedance passive layer formed during the oxidation process has significant influence on the deep cycle properties of the battery [2,3]. Additives are, therefore, often used to improve the properties of lead–calcium alloys. Tin and aluminum are widely used as additives. The addition of tin can improve the physical and chemical properties of a Pb–Ca alloy, typically reducing the thickness of the PbO passive film, and improving the conductive properties of the passive layer [4–8]. The addition of aluminum in the molten state can form an outer protective film of aluminum oxide, coating the electrode and preventing the loss of calcium [9].

Many studies [10–12] have focused on the mechanical properties, corrosion resistance and electrochemical properties of lead–calcium alloys in sulfuric acid solution, but the properties of its microstructure are rarely reported in China. Lakshmi's studies [10] have shown that the contents of calcium and tin are the main factors influencing the microstructure of Pb–Sn–Ca–Al alloys. However, high tin and high calcium lead–calcium alloys were still used as battery grids in lead-acid battery industry of China. There were more than 120 kinds of lead–calcium alloys (with different contents of calcium and tin) used to lead-acid batteries in Zhuzhou Smelter Group Co., Ltd. Inspired by Lakshmi's studies, the metallographic structures of Sn–Pb–Ca–Al alloys with varying compositions were observed in order to investigate the relationship between microstructure and alloy composition, plus the effect of microstructure on the properties of the alloys in this study. The composition of the alloy was adjusted in order to optimize the electrochemical properties. We hope the research results can provide a reference for the application of lead–calcium alloys in lead-acid battery industry of China.

---

* Corresponding author. Tel.: +86 20 39310183; fax: +86 20 39310183.
E-mail addresses: analchemlh@scnu.edu.cn (H. Li), sanven77@126.com (W.X. Guo), battery@scnu.edu.cn (H.Y. Chen), dfinlow@shawnee.edu (D.E. Finlow).

[1] http://www.scnu.edu.cn.

0378-7753/$ – see front matter © 2008 Elsevier B.V. All rights reserved.
doi:10.1016/j.jpowsour.2008.10.059

Table 1
Ingredients of the Sn–Pb–Ca–Al alloys.

Categories	Sample No.	Content (%)			Ratio values ($r = Sn/Ca$)	Size of particles (μm)
		Ca	Sn	Al		
Low-calcium–high-tin	1	0.074	1.56	0.02	21.08	240–467
Lead–calcium alloy	2	0.075	1.62	0.017	21.60	124–440
Low-calcium–medium-tin	3	0.072	0.91	0.02	12.64	71–260
Lead–calcium alloy	4	0.074	0.96	0.019	12.97	60–221
Medium-calcium–medium-tin	5	0.089	0.91	0.029	10.22	8–49
Lead–calcium alloy	6	0.085	0.76	0.034	8.94	9–46
Medium-calcium–low-tin	7	0.087	0.31	0.021	3.56	4–29
Lead–calcium alloy	8	0.095	0.23	0.029	2.42	4–27
High-calcium–medium-tin	9	0.109	0.72	0.021	6.61	5–31
Lead–calcium alloy	10	0.11	0.82	0.023	7.45	4–29
High-calcium–low-tin	11	0.116	0.15	0.026	1.29	6–30
Lead–calcium alloy	12	0.115	0.30	0.033	2.61	5–28
High-calcium–without	13	0.122	00	0.033	00	7–32
Lead–calcium alloy	14	0.124	00	0.031	00	6–31

2. Experimental

2.1. Equipment

A Nikon LV-UEPT polarizing microscope (Nikon, Japan); a PG-2 Metallographic polishing machine (Shanghai Metallographic Machinery Co., Ltd., China); a JSM-6380 Scanning electron microscope–energy dispersive X-ray spectrometer (SEM–EDS) (JEOL Electronics Company, Japan); an Autolab PGSTAT 30 electrochemical system (Eco-Chemie, The Netherlands); and a CHI660 electrochemical workstation (Shanghai Chenhua Co., Ltd., China) were utilized.

2.2. Chemical reagents

The sulfuric acid, hydrogen peroxide, acetic acid, ammonium molybdate, citric acid, and anhydrous ethanol used were of analytical reagent grade. Double distilled water was used in this study (self-made).

2.3. Procedure for treatment of the electrodes

The ingots of alloys were provided by Zhuzhou Smelter Group Co., Ltd., their chemical compositions were shown in Table 1. To prepare such alloys, the ingots of alloy were cut into square plate (20 mm length, 20 mm width, and 2 mm height) and cylindrical alloy (8.0 mm in diameter, and 16.0 mm length). The cylindrical-shaped castings were used as electrochemical electrodes. One end of the cylindrical-shaped alloys was welded to copper wire, and sealed by epoxy resin; the other end was polished with sandpaper to form the working electrode disc. The square plates were used for the corrosion experiments.

2.4. Procedure for metallographic testing

The properties of Sn–Pb–Ca–Al alloys depend mainly on the calcium and tin content in the alloy. The 14 types of lead–calcium alloy ingots provided by the Zhuzhou Smelter Plant are divided into 7 categories, according to the content of calcium and tin in the alloy. The ratio of the content of tin to calcium, r, and their particle size range are also provided in Table 1.

The square plate alloys were polished, successively using 800, 1200, and 2000 mesh sandpaper, until their surfaces were bright and had no obvious scratches. The diamond (W0.5) was used for final polishing, followed by double distilled water for rinsing, hydrogen peroxide and acetic acid (equal parts by volume) solution for chemical polishing, a citric acid and ammonium molybdate solution (15 g citric acid, 9 g ammonium molybdate, 90 g double distilled water) for etching, ethanol for cleaning, and drying. The metallographic structure of each sample was observed by both polarized light and scanning electron microscopy.

2.5. Pretreatment for electrochemical experiments

The electrode properties were tested in a three-electrode system using the Pb–Ca–Sn–Al alloy as the working electrode, Pt as the auxiliary electrode, Hg/Hg_2SO_4 as the reference electrode and a $1.28\ g\ cm^{-3}$ H_2SO_4 electrolyte. Before each measurement, the working electrode surface was gently polished on the abrasive papers (600, 1200, and 2000 mesh), and then washed with ethanol and

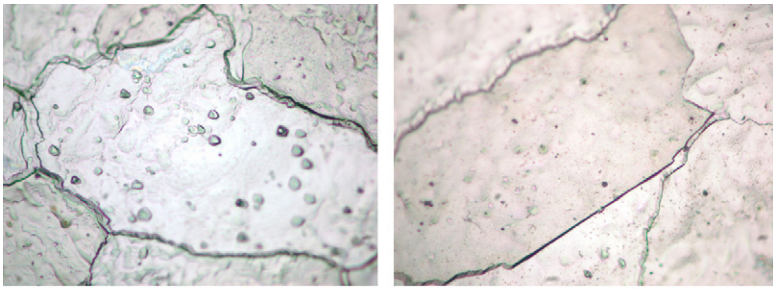
Sample 1 (500 X) $r = 21.08$ Sample 2 (500 X) $r = 21.60$

Fig. 1. Microstructures of the low-calcium–high-tin alloys.

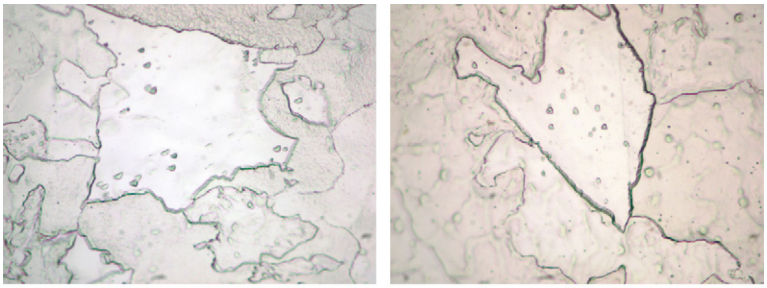

Sample 3 (500 X) $r = 12.64$ Sample 4 (500 X) $r = 12.97$

Fig. 2. Microstructures of the low-calcium–medium-tin alloys.

double distilled water. In order to remove the oxide produced during the polishing, the working electrode was polarized at −1.2 V for 10 min prior to each measurement.

3. Results and discussion

3.1. Metallographic structure

The metallographic structures of lead–calcium alloys with different ingredients are shown in Figs. 1–7 (500× magnification). The polarized light microscopy data analysis software was utilized to generate the grain size distributions of the various alloys provided in Table 1. Fig. 1 illustrates that the low-calcium–high-tin alloys (samples 1 and 2) had a massive coarse crystal structure with smooth and clear grain boundaries. Fig. 2 shows the coarse-grained structure of the low-calcium–medium-tin alloys (samples 3 and 4); the grains were slightly smaller, but did not change significantly when the content of tin in the alloy was reduced to about half that of the high-tin alloy. Fig. 3 indicates that the microstructure of the medium-calcium–medium-tin alloys (samples 5 and 6) clearly changed when the content of calcium was increased; the grain size was moderate and its distribution is irregular. Such irregular grain boundaries result from discontinuous deposition.

The microstructure of the low-calcium–high-tin alloys (samples 7 and 8) had more finely serrated grains, and a more uniform structure (Fig. 4), which is the typical lead–calcium alloy structure. The grains became smaller as the content of Sn in the alloy was reduced. Fig. 5 illustrates the microstructure of the high-calcium–low-tin alloys (samples 9 and 10), which had a smaller grain size with star- or square-shaped particles on the surface of the alloy. EDS analysis indicated that the particles appear to be Pb_3Ca (intermetallic compound). The microstructure of high-calcium–low-tin alloys (samples 11 and 12) had a refined microstructure similar to that of Fig. 5, with Pb_3Ca precipitation on the surface (Fig. 6). The microstructure of high-calcium–without-tin alloys (samples 13 and 14), provided in Fig. 7 illustrates that the grain boundary was irregular and serrated, with Pb_3Ca precipitation on its surface.

Evidently, Sn–Pb–Ca–Al alloy grain size is determined by the content of calcium and tin; the grains gradually becoming smaller with increasing calcium and decreasing tin content in the alloy. The size and shape of the grain are closely related to r (the ratio of tin to calcium in the alloy). The grain is: coarse, bulky, and smooth when r is between 12.64 and 21.85; moderate, with an irregular interface, when r is between 8.94 and 10.22; fine, with an irregular interface, plus a serrated-shape distribution, when r is between 0 and 7.45. Thus the alloy grain size is: small for $r < 9$; moderate for $r \sim 9$; coarse for $r > 9$.

Intermetallic compounds, identified as Pb_3Ca by EDS, are precipitated in high-calcium (Ca > 0.1%) alloys (Figs. 5–7). A peritectic reaction occurs in the lead–calcium alloy at 328.3 °C, when the solubility of calcium in lead is 0.1%. At room temperature the solubility of calcium in lead is 0.01%. During cooling, Pb_3Ca is transferred to the grain boundary from the supersaturated solid solution by the process of discontinuous precipitation, forming flake precipitation. Pb_3Ca creates an alkaline environment [13], accelerating the passivation of the grid and reducing the activity of the interface. This is one of the reasons for poor performance during the charge–discharge cycle. The presence of Pb_3Ca is primarily related to the content of calcium, and appears not to be related to the content of tin in the alloy. Therefore, in order to reduce the presence of intermetallic compounds, the content calcium of the alloy should be controlled at a lower level.

3.2. Energy dispersive spectrometer (EDS) analysis

The structure of the lead–calcium alloy grains can be observed by polarizing microscope, but the surface morphology and the distribution of elements on the surface is difficult to characterize by this method. Some precipitated intermetallic compounds, pure metal, and impurities can be found by scanning electron micro-

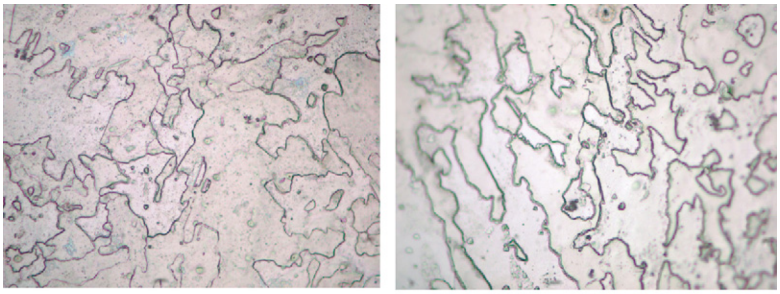

Sample 5 (500X) $r = 10.22$ Sample 6 (500 X) $r = 8.94$

Fig. 3. Microstructures of the medium-calcium–medium-tin alloys.

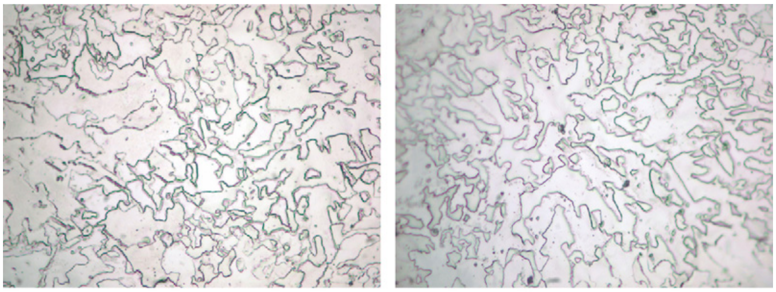

Sample 7 (500 X) $r = 3.56$ Sample 8 (500 X) $r = 2.42$

Fig. 4. Microstructures of the medium-calcium–low-tin alloys.

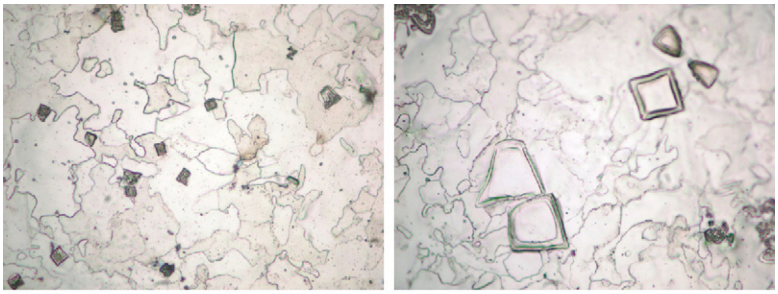

Sample 9 (500X) $r = 6.61$ Sample 10 (500X) $r = 7.45$

Fig. 5. Microstructures of the high-calcium–medium-tin alloys.

scope analysis. The components at these sites can be analyzed by EDS.

Figs. 8 and 9 are the EDS results for the butterfly- and square-shaped particles in the high-calcium alloys, respectively.

The content of calcium in these particles is very high, yet calcium can barely be detected around them, which indicates that calcium was enriched in these particles. We speculated that the particles are the intermetallic compound Pb_3Ca, as the particles were easily dissolved during the chemical corrosion experiments, and the EDS results show that there is a high content of calcium in the integrated grains (Fig. 9) and a low content of calcium in the particle (Fig. 10), indicating that calcium was lost in the process of dissolution.

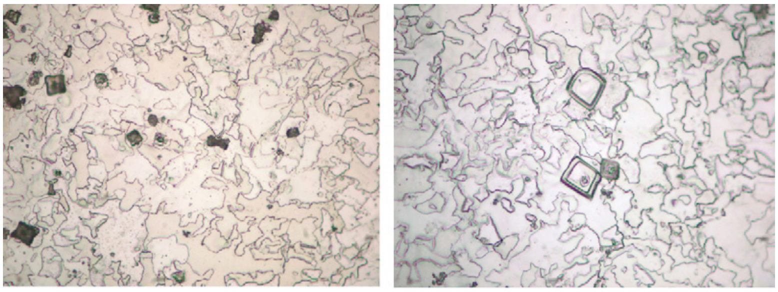

Sample 11 (500X) $r = 1.29$ Sample 12 (500X) $r = 2.61$

Fig. 6. Microstructures of the high-calcium–low-tin alloys.

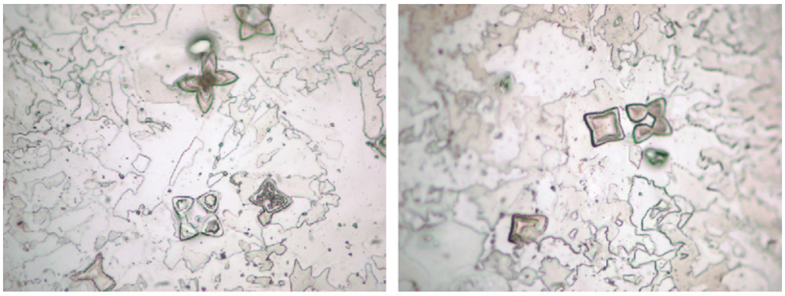

Sample 13 (500X) $r = 0$ Sample 14 (500X) $r = 0$

Fig. 7. Microstructures of the high-calcium–without-tin alloys.

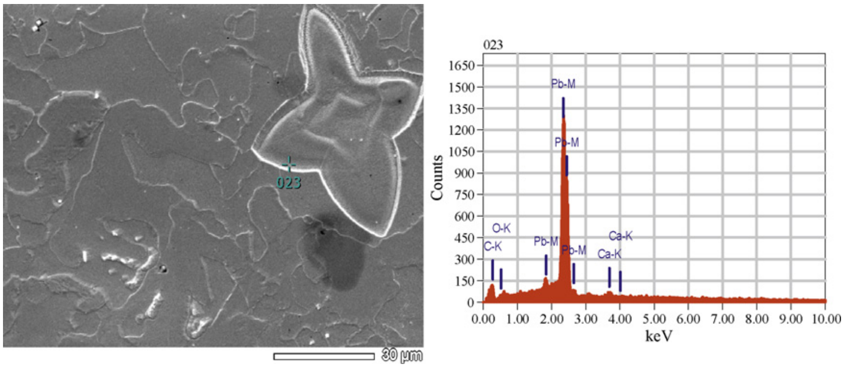

Fig. 8. EDS analysis of butterfly-shaped particles in the high-calcium alloys.

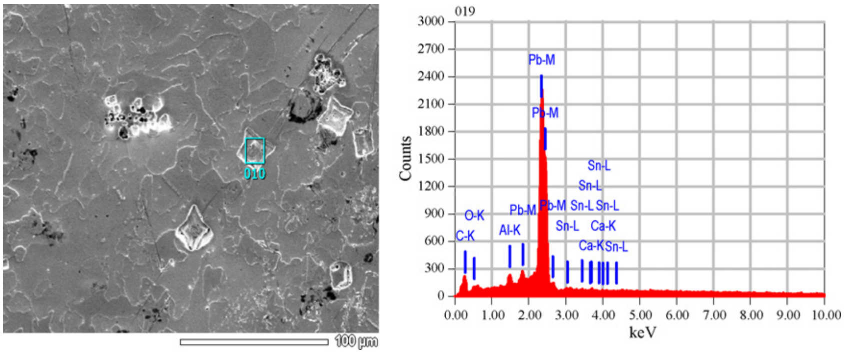

Fig. 9. EDS analysis of star-shaped particles in the high-calcium alloys.

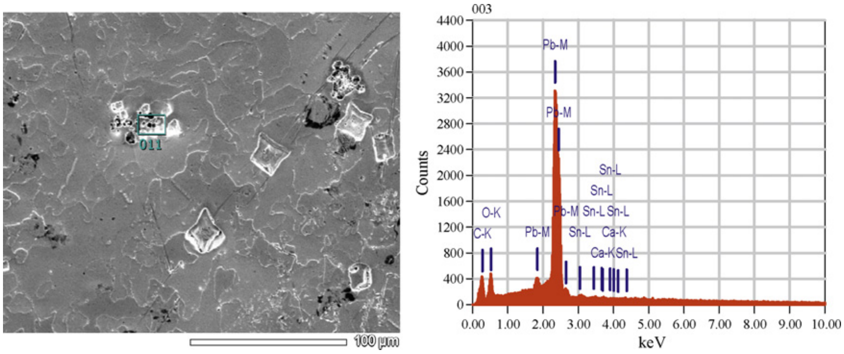

Fig. 10. EDS of the deliquescent star-shaped particles in the high-calcium alloys.

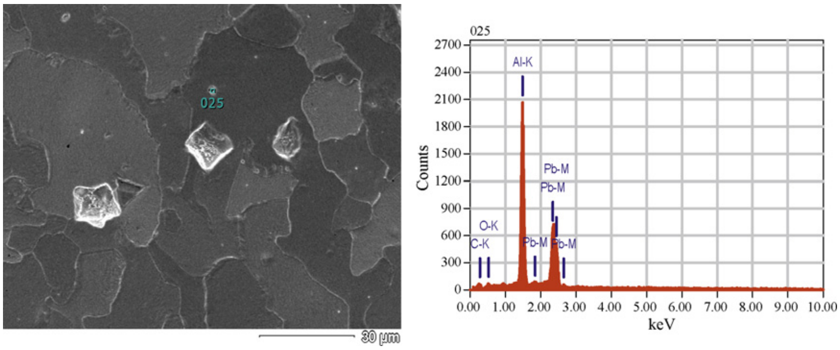

Fig. 11. EDS analysis of white particles found in the high-calcium alloys.

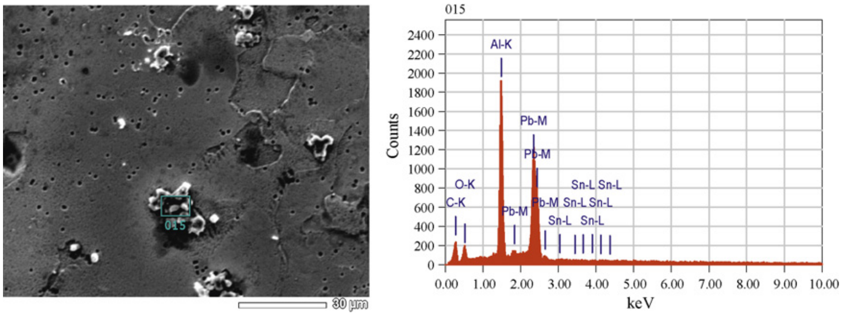

Fig. 12. EDS analysis of the congeries in the lead–calcium alloys.

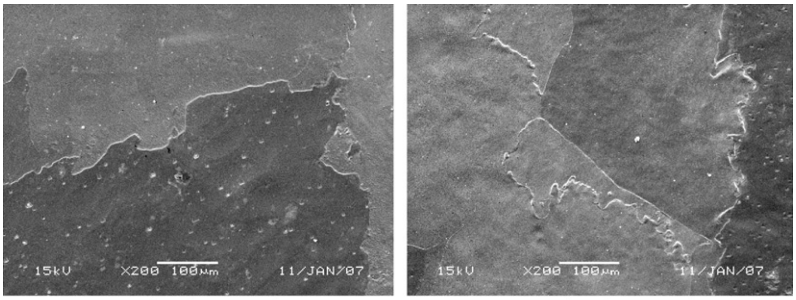

Sample 1 ($r = 21.08$) Sample 2 ($r = 21.60$)

Fig. 13. SEM images of the low-calcium–high-tin alloys.

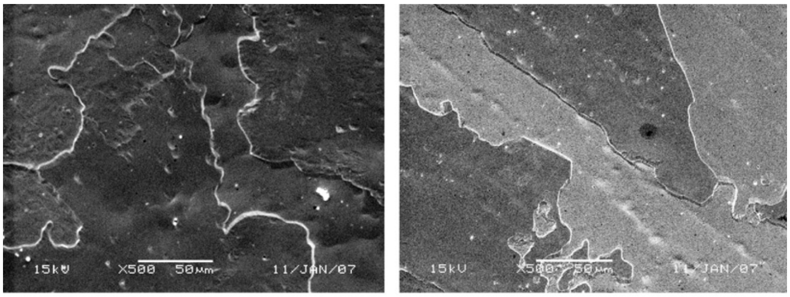

Sample 5 ($r = 10.22$) Sample 6 ($r = 8.94$)

Fig. 14. SEM images of the medium-calcium–medium-tin alloys.

We analyzed the small white grains (Fig. 11) and the congeries (Fig. 12) by EDS and found that they contained a high content of aluminum, thus we can speculate that these particles resulted from the segregation and enrichment of aluminum. The data of Table 2 show that the elements oxygen and carbon can be found at all sites, as a result of the etching of the lead alloy.

3.3. *Scanning electron microscopy (SEM)*

Fig. 13 provides the SEM image (200×) of the sample 1 and 2 alloys. Their r values are greater than 9, the grain surface is smooth, and the grain boundary is clean, regular, and has good corrosion resistance. There are many white deposits, determined to be aluminum, on their surface, with more white substance on the surface of sample 1 than on the surface of sample 2. Fig. 14 gives the SEM images of alloys 5 and 6. Their r values are about 9; there are coarse grains and slender grains in these alloys, and their grain boundaries lie somewhere between the regular and irregular states, indicating that the structure of the alloy is in a transitional state. There is little aluminum precipitation on their surface. Based on the results from Figs. 13 and 14, enrichment or precipitation of aluminum is not related to the content of aluminum in the alloy; it appears to occur at random. Therefore, the content of aluminum should be controlled in the range of 0.02–0.03% to avoid aluminum particle precipitation.

The SEM images of the samples 11 and 12 alloys are provided in Fig. 15. Their r values are less than 9, the content of calcium is greater than 0.1%, and there are many intermetallic compound particles uniformly distributed on the surface of alloy.

Comparing Figs. 11 and 12 (both with magnification 1000×), it appears that the size of the particles of intermetallic compound is

Table 2
Atomic percentage of various elements.

	Atomic percentage (%)					
	Pb	Ca	Sn	Al	C	O
Fig. 8	60.46	11.99	0.50	0.54	16.08	10.24
Fig. 9	59.63	6.29	0.48		25.28	8.32
Fig. 10	68.11	0.40	0.14		27.84	3.51
Fig. 11	12.12			66.27	15.04	6.57
Fig. 12	10.45		0.11	38.25	36.76	14.43

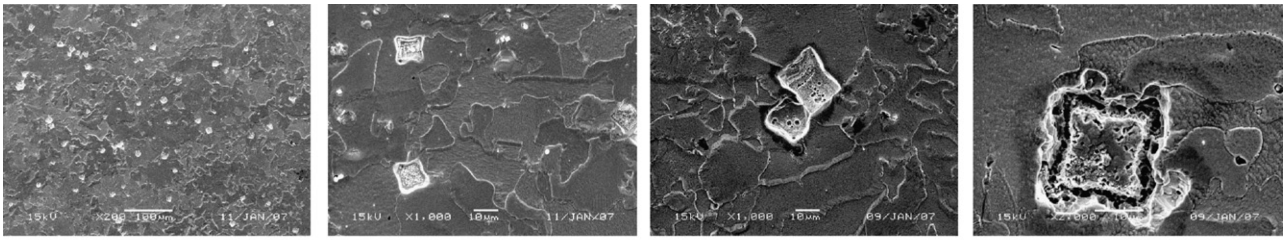

Sample 11 (r = 1.29) Sample 11 (r = 1.29) Sample 12 (r = 2.61) Sample 12 (r = 2.61)

Fig. 15. SEM images of the high-calcium–low-tin lead–calcium alloys.

not related to the composition of the alloys. At 2000× magnification, the phenomenon of intermetallic compound dissolution can be observed. We can speculate that Pb_3Ca is more prone to corrosion than the lead–calcium matrix, thus the sites of dissolved compounds will allow accelerated corrosion of the grid alloy. In order to improve the corrosion resistance of the positive grid alloy, the content of calcium should be less than 0.1%. However, in order to maintain an acceptable mechanical strength of the lead calcium alloy, the content of calcium should be greater than 0.07%, thus the optimal content of calcium in the alloy is 0.07–0.1%.

3.4. Electrochemical analysis

Metallographic, scanning electron microscopy, and EDS analysis indicated that the optimized contents of Ca and Al in positive grid alloys were 0.07–0.1% and 0.02–0.03%, respectively. The four alloys (samples 1, 3, 5, and 7), for which the content of Ca was 0.07–0.1%, and the value of *r* varied, were selected for further study to optimize the content of Sn in the Pb–Ca–Sn–Al alloy. Electrochemical properties were compared for alloys with different combinations of *r* value and Sn content. Because the addition of tin can improve the passive film ($PbO + PbO{\cdot}PbSO_4$) performance, the electrochemical properties of these types of alloys were compared by linear sweep voltammetry and electrochemical impedance spectrometry (EIS) when the passive film potential was 0.9 V.

3.5. Linear sweep voltammetry (LSV)

Fig. 16 presents the cathodic reduction curves after 1 h of the electrodes produced with alloys 1, 3, 5, and 7 at the oxide film formation potential of 0.9 V. There are two reduction peaks, *a* and *b*, which correspond to the Pb(II) ($PbO + PbO{\cdot}PbSO_4$) reduction to Pb and $PbSO_4$ reduction to Pb, respectively [14]. The peak currents and peak potentials of peaks *a* and *b* are given in Table 3. The data indicate that the peak potential of *a* in alloys 1, 3, and 5 is higher than that of alloy 7, which indicates that Pb(II) is more vulnerable to reduction and improves the activity of Pb(II) in the passive film. In addition, the peak currents of peak *a* in alloys 1, 3, and 5 are much lower than that of alloy 7, indicating that because only a small amount of Pb(II) was produced, growth of the passive film was inhibited. The peak currents of peak *b* for alloys 1, 3, and 5 are lower than that of alloy 7, which indicates that the small amount of Pb(II) produced can also inhibit the reduction of lead sulfate. The data indicate that the peak currents of peaks *a* and *b* of alloy 1 are very close to those of alloy 3; there is little difference in inhibitory effect between the two alloys

Table 3
The parameters of the peak potential and peak current for peaks *a* and *b* in the LSV test.

Electrodes	E_a (V)	I_a (mA cm^{-2})	E_b (V)	I_b (mA cm^{-2})
Alloy 1	−0.801	0.71	−1.03	0.96
Alloy 3	−0.803	0.74	−1.025	1.04
Alloy 5	−0.802	0.85	−1.027	1.13
Alloy 7	−0.889	1.36	−1.027	1.56

3.6. Electrochemical impedance spectra (EIS)

Fig. 17 presents the Nyquist plots for the anodic films formed on the electrodes with different *r* values at 0.9 V in sulfuric acid

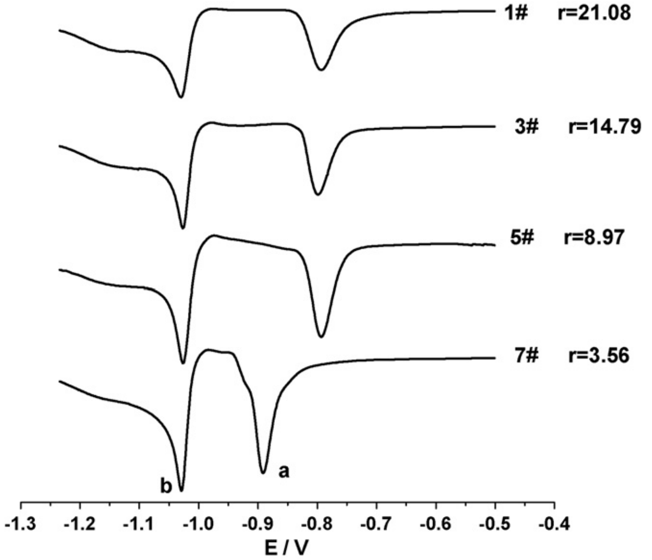

Fig. 16. The cathodic curves of the electrodes with different *r* values after oxidation for 1 h at Pb(II) growth potential in 1.28 g cm^{-3} H_2SO_4 solution.

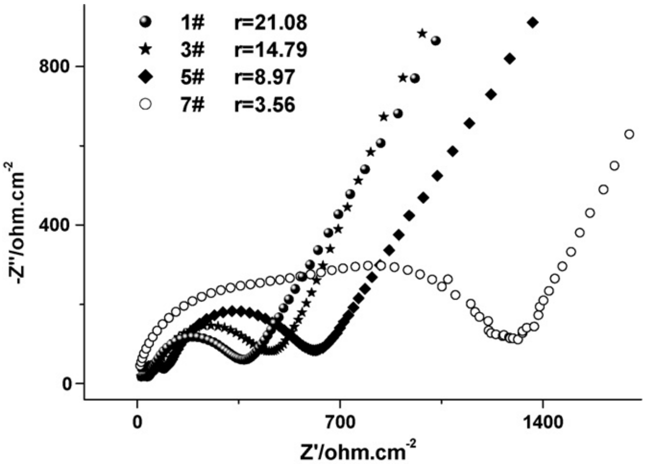

Fig. 17. Nyquist plots for the anodic films formed on the electrodes with different *r* values at 0.9 V in H_2SO_4 (1.28 g cm^{-3}) for 1 h.

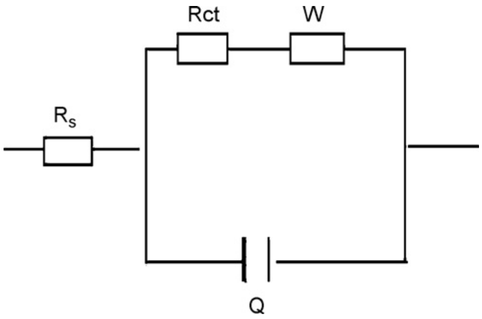

Fig. 18. The equivalent circuit used to fit the impedance data measured during the Pb(II) growth on the electrodes.

Table 4
The fitted values calculated from the impedance data of Fig. 17.

Electrodes	R_s ($\Omega\,cm^{-2}$)	R_{ct} ($\Omega\,cm^{-2}$)	Q	W	n
Alloy 1	12.84	397	0.562	0.229	0.56
Alloy 3	3.28	447	0.625	0.134	0.72
Alloy 5	13.2	554	0.486	0.162	0.69
Alloy 7	35.9	1210	0.041	0.116	0.61

solution (1.28 g cm^{-3}) for 1 h. It shows that the reaction is controlled by charge-transfer at high-frequencies and by ion-diffusion at low-frequencies. Fig. 18 provides the equivalent circuit [15,16] used to fit the impedance data measured during the Pb(II) growth on the electrodes; R_s is the resistance of the solution, R_{ct} is the charge-transfer resistance, Q is the capacitance of oxide film, and W is the Warburg impedance. The data obtained from this simulated circuit are presented in Table 4, and indicate that the R_{ct} values of alloys 1, 3, and 5 are much lower than that of alloy 7, and implies that there is little Pb(II) produced in alloys 1, 3, and 5. Also, the R_{ct} value of alloy 1 is very close to that of alloy 3, indicating that the influence on the passive film of the r value has reached its limit. According to the results from LSV and EIS, when r is greater than or equal to 9, the alloys inhibit growth of the passive film, but for $r > 9$, the inhibitory effect does not improve with increasing r. The inhibitory effect on passive film growth of alloy 1 is very close that of alloy 3. For $r > 15$, the impact of the content of tin on the passive film growth tends to reach a limit, thus the optimal range of r is 9–15. In the past, researchers generally thought that a higher tin content enhanced the inhibitory effect. However, according to the range of r values in our experiment, the appropriate content of tin in positive grid alloys should be $0.8 \sim 1.1\%$. Adding an excessive amount of tin would increase the cost of alloy, but the inhibitory effect would apparently not improve.

4. Conclusions

Sn–Pb–Ca–Al alloy grains gradually became smaller as the content of calcium increased and the content of tin decreased. When the r value was about 9, the particle size was moderate and the grain boundary was irregular. For $r > 9$, the particle size was massive and the grain boundary had a regular shape. When $r < 9$, the particles were small and the grain boundaries were irregular. In order to improve the binding force between the positive grid and the active material, it is necessary to increase the grain size and the thickness of corrosion layer, thus r values >9 are the most suitable for positive grid alloys. The experimental results were consistent to that of the Ref. [10].

Stellate, bulk and butterfly-shaped irregular particles often appeared in lead–calcium alloys when the content of calcium was >0.1%. The particles were ascertained to be the intermetallic compound Pb_3Ca by EDS. However, this phenomenon did not occur in lead–calcium alloys for calcium content <0.1%. The intermetallic compound Pb_3Ca is associated with the content of calcium and has no apparent relationship with the content of Sn. The appearance of Pb_3Ca would create an alkaline environment, which would accelerate the passivation of the grid interface. In addition, the intermetallic compound has poor corrosion resistance and will weaken the corrosion resistance of the grid alloy. The content of calcium in the alloy should therefore be controlled at a lower level; 0.07–0.1% appears to be optimum.

Aluminum is prone to segregation and enrichment in lead–calcium, the phenomenon appears to be random, and independent of the content of aluminum in the alloys. The content of aluminum in an alloy should therefore be controlled in the range 0.02–0.03% to avoid the appearance of aluminum particles.

The results from LSV and EIS show that the alloys can inhibit the growth of a passive film for $r \geq 9$. The experimental results indicate that the appropriate content of tin in a positive grid alloy is 0.8–1.1%.

Acknowledgements

This work was funded by the Program Foundation of Science of Guangdong Province (No. 2005A10701002) and the Significant Program Foundation of Science of Guangzhou (No. 2005Z2-D2011).

References

[1] S.R. Li, Lead and Lead Alloy, Central South University Publishing House, Hunan, 1996.
[2] S. Zhong, H.K. Liu, S.X. Dou, M. Skyllas-Kazacos, J. Power Sources 59 (1996) 123–129.
[3] N. Koura, T. Sakaue, J. Power Sources 69 (1997) 69–74.
[4] N. Bui, P. Mattesco, P. Simon, N. Pebere, J. Power Sources 73 (1998) 30–35.
[5] P. Simon, N. Bui, N. Pebere, F. Dabosi, J. Power Sources 53 (1995) 163–173.
[6] C.S. Brini, C.M. Metikos-Hukoui, C.R. Babi, J. Power Sources 55 (1) (1995) 19–24.
[7] P. Mattesco, N. Bui, et al., J. Power Sources 64 (1997) 21–27.
[8] X.W. Yang, Y.G. Tang, J.B. Shen, Battery Bimonthly 3 (2006) 237–239.
[9] L. Liu, L.S. Yang, Chin. J. Power Sources 4 (1994) 29–34.
[10] C.S. Lakshmi, J.E. Manders, et al., J. Power Sources 73 (1) (1998) 23–29.
[11] H. Giess, J. Power Sources 53 (1) (1995) 31–43.
[12] R. Miraglio, L. Albert, A. El Ghachcham, J. Steinmetz, J.P. Hilger, J. Power Sources 53 (1) (1995) 53–61.
[13] D.A.J. Rand (Editor-in-chief), Y.L. Guo (Translator). VRLAB [M], Beijing: Machinery Industry.
[14] H.T. Liu, C.X. Yang, H.H. Liang, J. Yang, W.F. Zhou, J. Power Sources 103 (2) (2002) 173–179.
[15] X.G. Hu, D.Y. Lin, Chin. J. Power Sources 28 (3) (2004) 139–141.
[16] X.G. Hu, D.Y. Lin, Y.F. Bao, Y. Wang, Z.H. Luan, Battery Bimonthly 33 (3) (2003) 139–141.